

ARCHITECTED MATERIALS

3D polycatenated architected materials

Wenjie Zhou^{1*}, Sujeeka Nadarajah¹, Liuchi Li^{2,3}, Anna Guell Izard⁴, Hujie Yan¹, Aashutosh K. Prachet¹, Payal Patel¹, Xiaoxing Xia^{4*}, Chiara Daraio^{1*}

Architected materials derive their properties from the geometric arrangement of their internal structural elements. Their designs rely on continuous networks of members to control the global mechanical behavior of the bulk. In this study, we introduce a class of materials that consist of discrete concatenated rings or cage particles interlocked in three-dimensional networks, forming polycatenated architected materials (PAMs). We propose a general design framework that translates arbitrary crystalline networks into particle concatenations and geometries. In response to small external loads, PAMs behave like non-Newtonian fluids, showing both shear-thinning and shear-thickening responses, which can be controlled by their catenation topologies. At larger strains, PAMs behave like lattices and foams, with a nonlinear stress-strain relation. At microscale, we demonstrate that PAMs can change their shapes in response to applied electrostatic charges. The distinctive properties of PAMs pave the path for developing stimuli-responsive materials, energy-absorbing systems, and morphing architectures.

Previously studied architected materials have mostly been designed with rigidly connected truss- (1, 2), plate- (3, 4), or shell-based lattices (5, 6) that derive effective bulk properties from the construct of periodically repeating unit cells (7, 8) or disordered architectures (9, 10). They can display remarkable behaviors, for example, showing high strength while being lightweight (2, 11), negative Poisson's ratios (12, 13), and shear-normal coupling (14, 15). Depending on the geometry of their interior structure, they exhibit unusual or extreme mechanical properties (2, 11), such as large reconfigurability (16–20), multistable responses (21, 22), and nonlinear elastic deformations (23, 24). In some realizations, architected materials behave like fluids—for example, in pentamode materials, which exhibit a near-zero shear response (25, 26). Granular crystals are a type of architected materials that consist of regular arrays of closely packed elements that interact elastically (27, 28). They also present rich mechanical properties, such as geometrical hardening (29) and nonlinear wave propagation (28), which emerge from the shape of the individual particles, their topological arrangement, and the particles' chemical composition. However, in the absence of boundary confinement, granular crystals are not cohesive because the particles are not held together by binders and they offer no resistance in tension.

An emergent family of architected materials are topologically interlocked fabrics, consisting of layers of two-dimensional (2D) concatenated particles, like chainmails used in

medieval armors, which have been shown to support tunable stiffness and controllable shape morphing (30, 31). We integrated the principle of polycatenation (32–34) into 3D architected materials that we fabricated at the macro- and microscales. Unlike chainmail, 3D polycatenated structures present interlayer linkages that lead to distinctive 3D strain redistribution, interlayer cohesiveness, and tunable energy absorption. The vast design space of 3D architected materials offers unprecedented opportunities to tailor mechanical properties (35).

Here, we propose a design framework for 3D concatenated structures with designated network topologies, to create interlocking arrangements of discrete ring or cage particle building blocks with controllable kinematic degrees of freedom (DOF). Such units are symmetrically catenated with their neighbors, which are free to move relative to each other within the bound of the interlocking mechanisms. We also propose a design strategy to translate continuous graph topologies, such as crystalline lattices (36), into their polycatenated counterparts and demonstrate the realization of 3D polycatenated architected materials (PAMs) from selected building blocks. We show how local variations in the particles' geometry affect the internal DOF, which, in turn, control the global deformability and effective response of the bulk. Because of the discrete nature of the particle-particle interactions in PAMs, their global mechanical behavior transitions from fluid-like to solid-like and from shear-thinning to shear-thickening, as a function of the applied loading. PAMs are resilient to cyclic loading and have tunable energy absorption, with scalable responses that persist at both the macro- and microscales. The characteristic behavior of PAMs arises from strong surface interactions between adjacent particles, for example, in contacts and relative sliding. These interactions can be further leveraged at smaller

scales by increasing the surface-to-volume ratio of the samples. To verify this hypothesis, we fabricated microscale PAMs and demonstrated their ability to rapidly and reversibly adapt their shapes in response to electrostatic charges.

Design approach for PAMs

I. Conversion of continuous graph topologies into PAMs

Traditional lattice structures can be mapped into continuous topological networks that consist of nodes and connections (Fig. 1A). Starting from a chosen crystalline network, we created periodically entangled toroidal, polygonal, or polyhedral caged particles (hereafter referred to as “particles”) that can be tessellated into PAMs. The process begins by identifying node symmetries in the continuous networks and aligning them with particles that possess these symmetries (Fig. 1B). These particles interlink with adjacent ones, replicating the original network connections (Fig. 1, A to C). Thanks to the enormous database of crystallographic symmetries, topological networks from databases such as the Reticular Chemistry Structure Resource (RCSR) (36) can be transformed into polycatenated analogs (fig. S1). A single node can be represented by using particles with various shapes, such as polyhedral wireframes, polygon clusters, or torus clusters (Fig. 1D). Depending on the nature of the constituent units, the topologies of resulting polycatenated architectures exhibit substantial variations (Fig. 1E).

II. Generating 3D PAMs from prescribed particle geometries

A given particle shape [e.g., cuboctahedron (CO)] can exhibit multiple symmetry axes (Fig. 1F), leading to several potential catenation environments (Fig. 1, G to I). By utilizing these catenations singularly or in combination, we can create a variety of PAMs (Fig. 1, J to M), each with its own global topology. We used a tripartite naming scheme, X-*n*-abc, for easy identification: “X” for the network topology (table S2), “*n*” for the number of concatenations per particle, and “abc” for the particle shape, either in full (lowercase letters) or as an acronym (uppercase letters). As an example, the label D-4-TET (Fig. 1C) denotes a polycatenated diamond network (D) constituted from tetrahedral (TET) wireframes that interlock corner-to-corner with four neighboring particles (4).

Mechanical characterization of PAMs

We designed $N \times N \times N$ arrays (where N is the number of unit cells consisting of one or more interlocked particles; see table S1) leading to different PAM geometries and topologies. We fabricated them by using additive manufacturing with a brittle acrylic polymer (37). We selected eight types of representative PAMs, four

¹Division of Engineering and Applied Science, California Institute of Technology, Pasadena, CA, USA. ²Department of Civil and Environmental Engineering, Princeton University, Princeton, NJ, USA. ³Hopkins Extreme Materials Institute, Johns Hopkins University, Baltimore, MD, USA. ⁴Lawrence Livermore National Laboratory, Livermore, CA, USA.

*Corresponding author. Email: zhouw@caltech.edu (W.Z.); xia7@lnl.gov (X.X.); daraio@caltech.edu (C.D.)

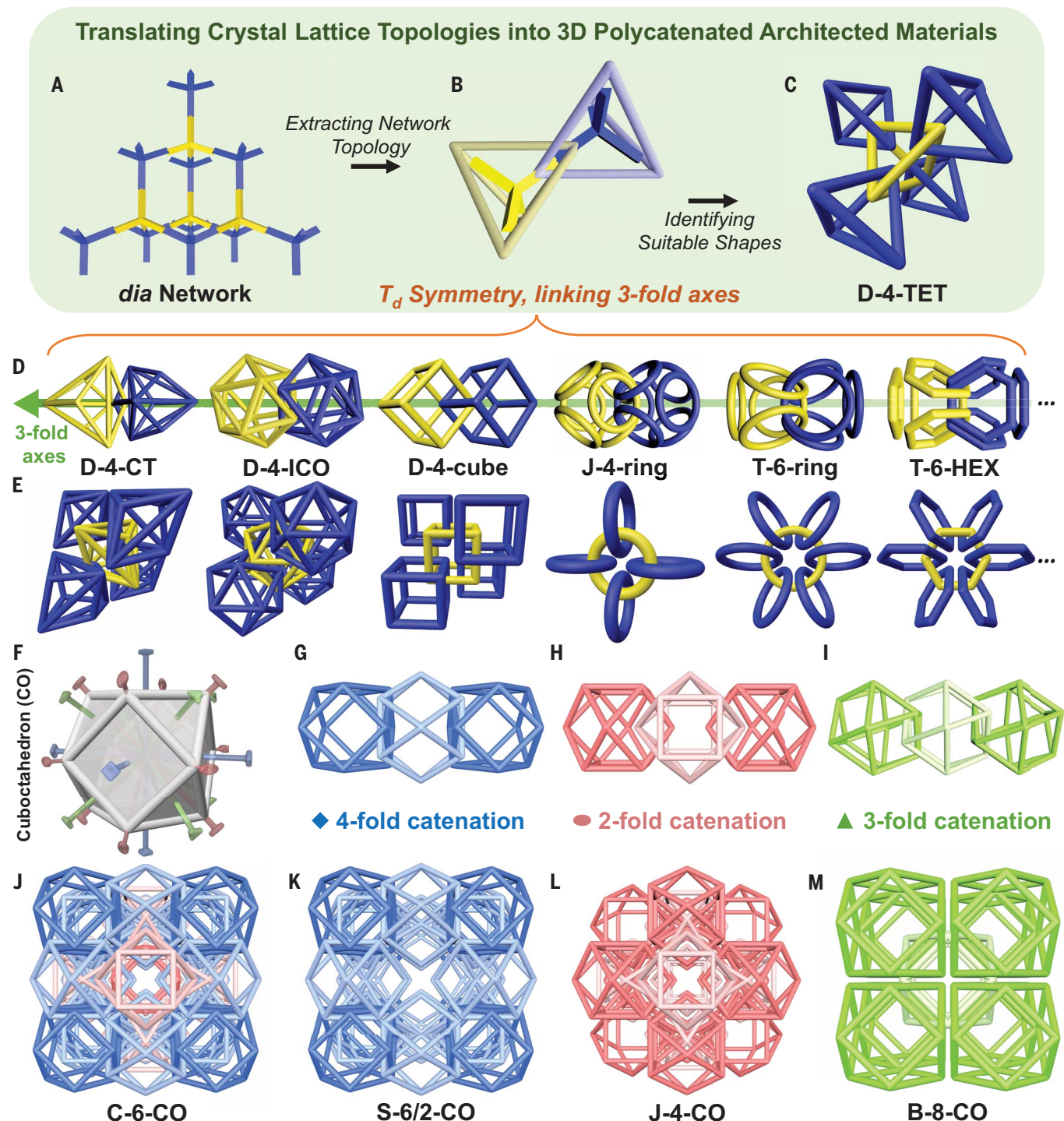


Fig. 1. Design strategy for PAMs. (A to E) A typical design workflow of PAMs from a designated network: (A) Network of the *dia* topology. (B) Essential nodes and their connections with adjacent nodes in the *dia* network. Each pair of nodes are mapped with two tetrahedral particles catenating their vertices, while aligning their threefold axes. (C) An extended D-4-TET PAM composed of tetrahedral particles. (D) An array of exemplary PAM variants in addition to the catenated tetrahedra, namely Catalan tetrahedra (D-4-CT), icosahedra (D-4-ICO), cubes (D-4-cube),

octahedrally arranged six-ring clusters (J-4-ring), tetrahedrally arranged four-ring clusters (T-6-ring), and tetrahedrally arranged four-hexagon clusters (T-6-HEX). The green line highlights the threefold symmetrical axis. (E) A series of extended PAMs corresponding to the configurations from (D). (F to M) Generation of PAMs from designated particle geometry: (F) to (I) show a cuboctahedron (CO), catenated through its fourfold (blue), threefold (green), and twofold (red) axes. (J) to (M) show expanded PAMs from the catenations illustrated in (G) to (I).

composed of 2D particles (fig. S4, A to D) and four composed of 3D particles (fig. S4, E to H). After fabrication and removal of support mate-

rial, the PAMs relaxed under gravity and the originally ordered and periodic microstructure became irregular (Fig. 2, A to G). Such gravity-

induced shape deformations (hereafter referred to as “relaxations”) of PAMs are highly dependent on their domain boundaries (e.g., spherical;

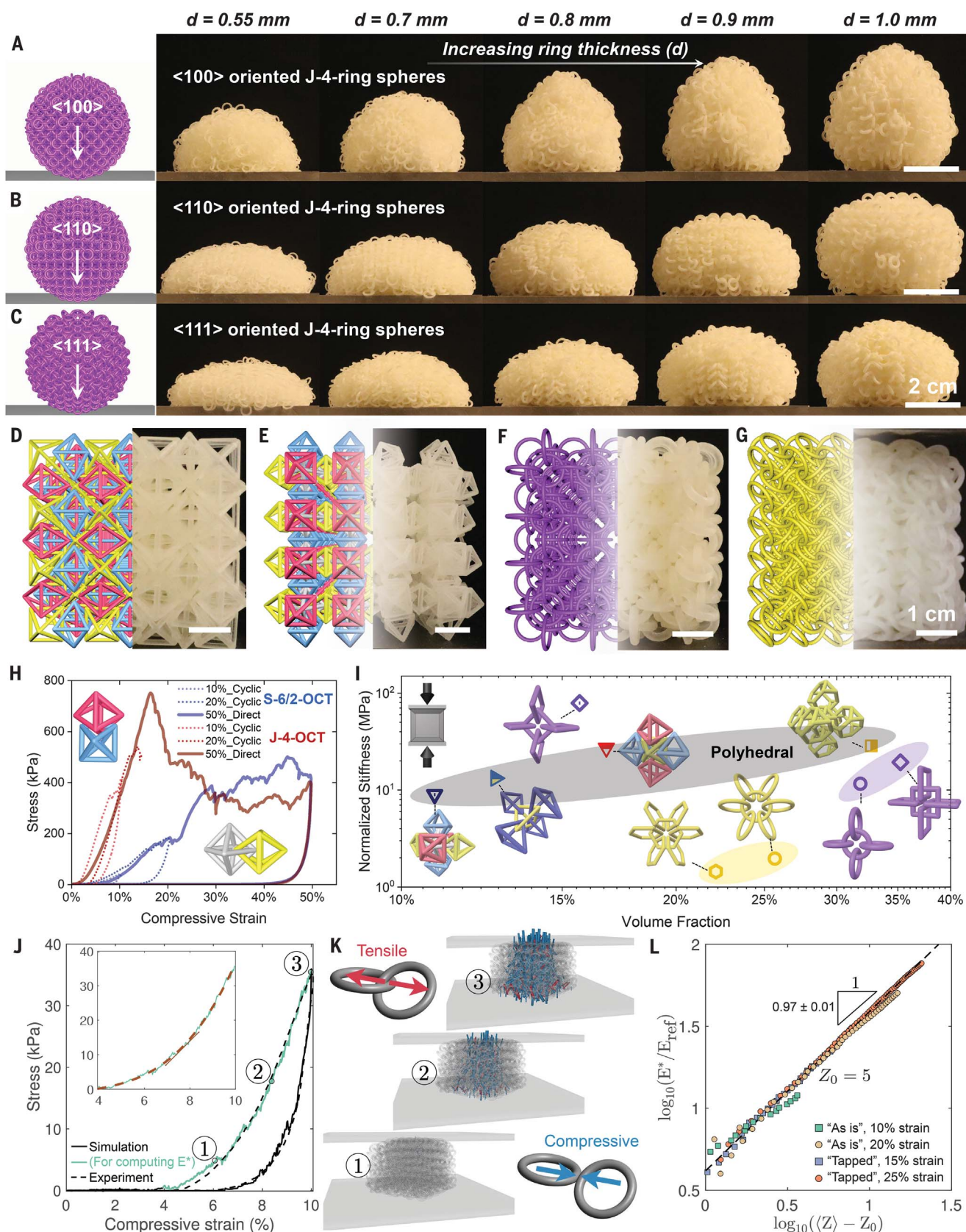


Fig. 2. Gravity-induced relaxation and uniaxial compression of PAMs. (A to C) Relaxation of a series of J-4-ring PAMs with spherical domain boundaries,

placed on a flat surface. When oriented along the <100> (A), <110> (B), and <111> (C) crystallographic axes, they show different relaxed outline shapes.

Scale bar, 2 cm. **(D to G)** Illustration and corresponding photos of expanded J-4-OCT, S-6/2-OCT, J-4-ring, and T-6-ring PAM samples. Scale bars, 1 cm. **(H)** Stress-strain plots of J-4-OCT and S-6/2-OCT PAMs under uniaxial compression. **(I)** Summary of normalized stiffness, calculated as the slope of the stress-strain curve (via linear fitting in the 5 to 10% strain range) and normalized by the measured volume fraction, plotted against the measured volume fractions. **(J)** A comparison of the response of a T-6-ring sample under uniaxial compression between experiment and LS-DEM simulation result. The inset shows the calculation of E^* by fitting a

polynomial to the simulated stress-strain response during the loading phase. **(K)** A visualization of the contact forces (blue being compressive forces and red being tensile forces) at three selected loading stages [see (J)]. Each contact force is represented by a cylinder whose orientation is the force vector direction and whose length and radius are scaled according to the force magnitude. **(L)** Relation between E^* and $\langle Z \rangle - Z_0$ for four simulations considering different preloading configurations and loading-strain ranges. All data can be reasonably represented by a power-law scaling (black dashed line) by setting $Z_0 = 5$.

Fig. 2, A to C) and on the particle-to-particle clearance. For mechanical characterization, we designed cubic samples with sides of about 50 mm (Fig. 2, D to G, and fig. S4) and measured their designed and relaxed dimensions, as summarized in table S1.

To characterize their mechanical responses, we conducted quasistatic uniaxial compression tests, simple shear tests, and rheology tests under different loading conditions. The mechanical response of PAMs emerges from a complex interplay of interactions across scales, ranging from (i) μm -scale interparticle contacts, (ii) mm-scale particle deformation (e.g., bending, buckling, and fracture), (iii) meso-scale layer-by-layer collapse, and (iv) cm-scale global deformations. Initially, all loadings induce the rearrangement of particles within the available kinematic DOF and the redistribution of stresses within the volume, without damage to the particles. However, the rearrangement of the particles leads to a bulk deformation of PAMs, which persists even after the removal of the external loads. As the particles reach a jammed state, further spatial reconfiguration becomes untenable. Beyond jamming, continued compressive forces result in the deformation, damage, and fracture of the particles.

Under uniaxial compression (Fig. 2H; figs. S6, A to F, and S7; and movie S2), all samples exhibit a nonlinear stress-strain behavior with substantial loading and unloading hysteresis (energy absorption). This hysteric stress-strain relationship is likely influenced by three distinct mechanisms: (i) the rearrangement of catenated particles, (ii) the presence of friction at the contact, and (iii) at larger strains, particle deformation and damage. After relaxation, the arrangement of the particles (i.e., their position and orientation) in PAMs is intrinsically disordered and varies from experiment to experiment. However, we observed that PAMs present consistent values of effective stiffness within a statistical distribution in the range of 10%.

A particularly interesting observation is the strain-stiffening response during the loading phase (Fig. 2J), which is reminiscent of the response of classical granular systems (38). To understand and quantify the role of dynamic contact chains within PAMs, we performed level-set discrete element method (LS-DEM) (39, 40) simulations with particles of arbitrary shapes (30, 41). We first analyzed the response of a T-6-

ring sample, subjected to uniaxial compression (37). Experimentally, under cyclic compression at lower strains, PAMs show a reduced peak stress and a hysteretic response with a progressively smaller area, then stabilize into a steady-state response after the first few cycles (fig. S7).

Within the small to moderate strain regime (e.g., no particle fracture), our numerical simulation quantitatively captured the steady-state stress-strain response (see Fig. 2J for an example). From the simulation result, we further calculated the apparent compressive modulus (E^*) at each loading step by fitting a polynomial to the stress-strain curve during the loading phase (Fig. 2J, inset). As the compression progressed, we observed that the T-6-ring PAM “densified” as more contacts (both tensile and compressive ones) formed among particles (Fig. 2K) and carried larger contact forces (indicated by thicker and longer blue and red lines in Fig. 2K). To relate the macroscale strain-stiffening response with the particle-scale “densification” process, we plotted E^* as a function of $\langle Z \rangle - Z_0$, where $\langle Z \rangle$ is the mean contact number (summing over cohesive and compressive ones) and Z_0 is the minimal contact number per particle for the sample to become structurally rigid (37, 42). Z_0 depends on many factors, such as particle friction, geometry, and catenation topology, and is unknown for these catenated granular systems. Nevertheless, we find that picking $Z_0 = 5$ can collapse data from different preparation protocols and loading strain ranges (Fig. 2L), which follows a power-law scaling as predicted by the critical phenomenon of jamming phase transition (42). In this case, the scaling exponent is very close to 1, and is obtained by fitting a second-order polynomial to the stress-strain curve to get E^* . This result, together with additional particle-scale analysis based on granular physics (fig. S11), suggests that the (small-strain) mechanics of PAMs share many features with that of classical granular materials. However, these LS-DEM simulation-based analyses will fail when particles deform or fracture.

Unlike other architected materials, PAMs exhibit a notable ability to adjust their interparticle arrangements in response to external loads, a characteristic also found in granular systems. This particle rearrangement leads to two mechanical regimes, which appear under all deformation modes: (i) a fluid-like response, with a vanishing shear modulus, linked to rela-

tive particle motion; and (ii) a solid-like response, characterized by particle deformation, beyond the jamming transition. To describe the fluid-like mechanical response, we conducted simple shear and rheology tests on J-4-ring and T-6-ring samples (Fig. 3, A and B). These PAMs were selected because they are composed of toroidal particles, which have greater kinematic DOF. To control testing conditions, we fabricated samples that incorporated top and bottom gripping plates (Fig. 3, A and B, and fig. S5).

Under shear loads, both J-4-ring and T-6-ring samples demonstrated a plateau region with force values close to zero, indicative of a fluid-like behavior (Fig. 3, C and F, and movie S3). Beyond a critical strain, these plateaus then transitioned to a quasilinear elastic region, typical of solid-like behavior. This transition can be correlated to the reduced DOF between rings, which jam under external tensile, compressive, or shear loads. The fluid-like and solid-like regimes can be programmed by designing the catenation topologies and particle geometries.

To further understand this fluid-solid duality, we characterized the rheological properties (37) of cylindrical-shaped PAM samples (Fig. 3B and movie S4). In oscillatory amplitude sweep experiments (Fig. 3, D and G), the J-4-ring and T-6-ring samples initially displayed a decrease in storage modulus (G'), loss modulus (G''), and complex viscosity (η^*) with increasing torsional strain. Upon reaching the critical jamming strain observed in simple shear tests, all three parameters began to increase (43). In the oscillatory frequency sweep experiments (Fig. 3, E and H), both J-4-ring and T-6-ring samples exhibited an unusual inflection in viscosity at high angular frequency. When subjected to torsional strains below their respective jamming transition thresholds, a notable transition from shear-thinning to shear-thickening was observed with increasing oscillation angular frequency. In the latter part of the shear-thickening phase, the substantial increase in viscosity is likely influenced by the inertia effects of particles under high-frequency oscillation conditions. Although both shear-thinning and shear-thickening behaviors have been observed in various materials (43, 44), they have not been reported concurrently in the same material, particularly with the observed pronounced reduction in viscosity followed by a substantial increase, as a function of both angular frequency or torsional strain.

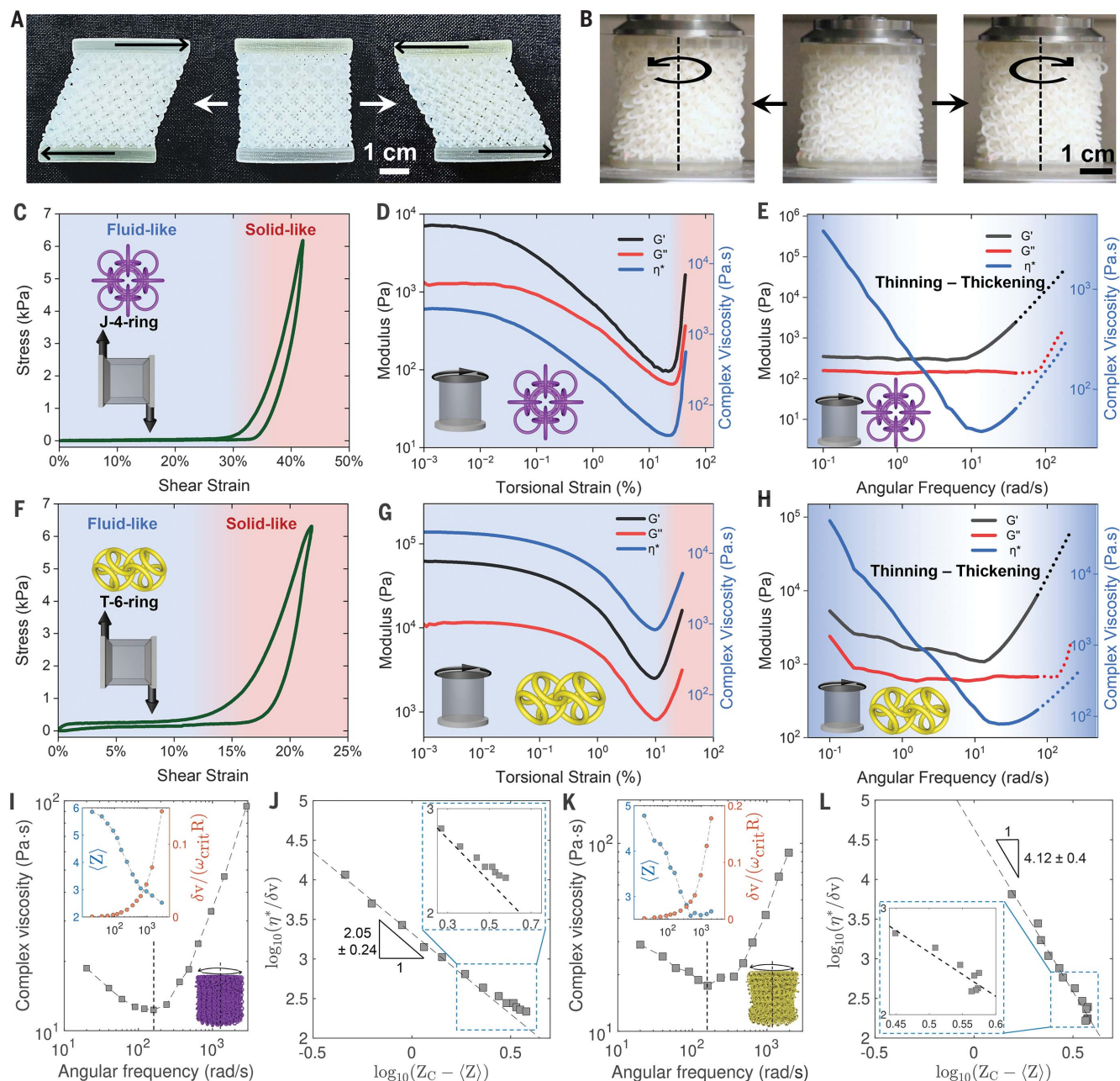


Fig. 3. Shear and rheology test of PAMs. (A and B) PAM samples in shearing and rheological test, showing the deformation in response to corresponding loads. (C and F) Stress-shear strain results for J-4-ring (C) and T-6-ring (F) PAMs, showing the transition from a fluid-like to solid-like regime with the increase of shear strain. (D, E, G, and H) Rheology results of J-4-ring (D) and T-6-ring (G) PAMs under oscillatory amplitude sweep (E) and frequency sweep (H), with plots of storage modulus (G'), loss modulus (G''), and complex viscosity (η^*) as a function of torsional strain and angular frequency. Dotted lines indicate the region where the tests were significantly affected by the instrument inertia effects. The blue shaded area in (C), (D), (F), and (G) indicates the region where the PAMs exhibit fluid-like behavior, transitioning to solid-like behaviors as

indicated by the red shaded area. (I and K) Simulation results of the variation of η^* as a function of angular frequency for J-4-ring (I) and T-6-ring (K) cylindrical samples. Insets show the mean contact number, $\langle Z \rangle$ (left axis), and normalized granular temperature, $\delta v / (\omega_{crit} R)$ (right axis), as a function of angular frequency. Here, ω_{crit} is the angular frequency at which the inflection of η^* occurs in our simulations and R is the radii of the sample, used only for making δv dimensionless. (J and L) Simulation results of the variation of $\eta^*/\delta v$ as a function of $Z_c - \langle Z \rangle$ for the J-4-ring (J) and T-6-ring (K) cylindrical samples. The black dashed lines are power-law fits using simulation data before the inflection of η^* . Insets show a magnified visualization of the main plot including a portion of the data after the inflection of η^* .

To better understand this unusual frequency-dependent thinning-to-thickening transition, we modeled the response of PAMs using the LS-DEM. We focused on modeling the rheological

experiments and on the inflection of η^* with increasing angular frequency. Because the mechanical deformation of each particle is minimal compared with the translation observed in their

rigid body motion (e.g., rearrangement) in the experiments, we modeled the rings as rigid particles. We used LS-DEM to model sweep experiments for both J-4-ring and T-6-ring samples.

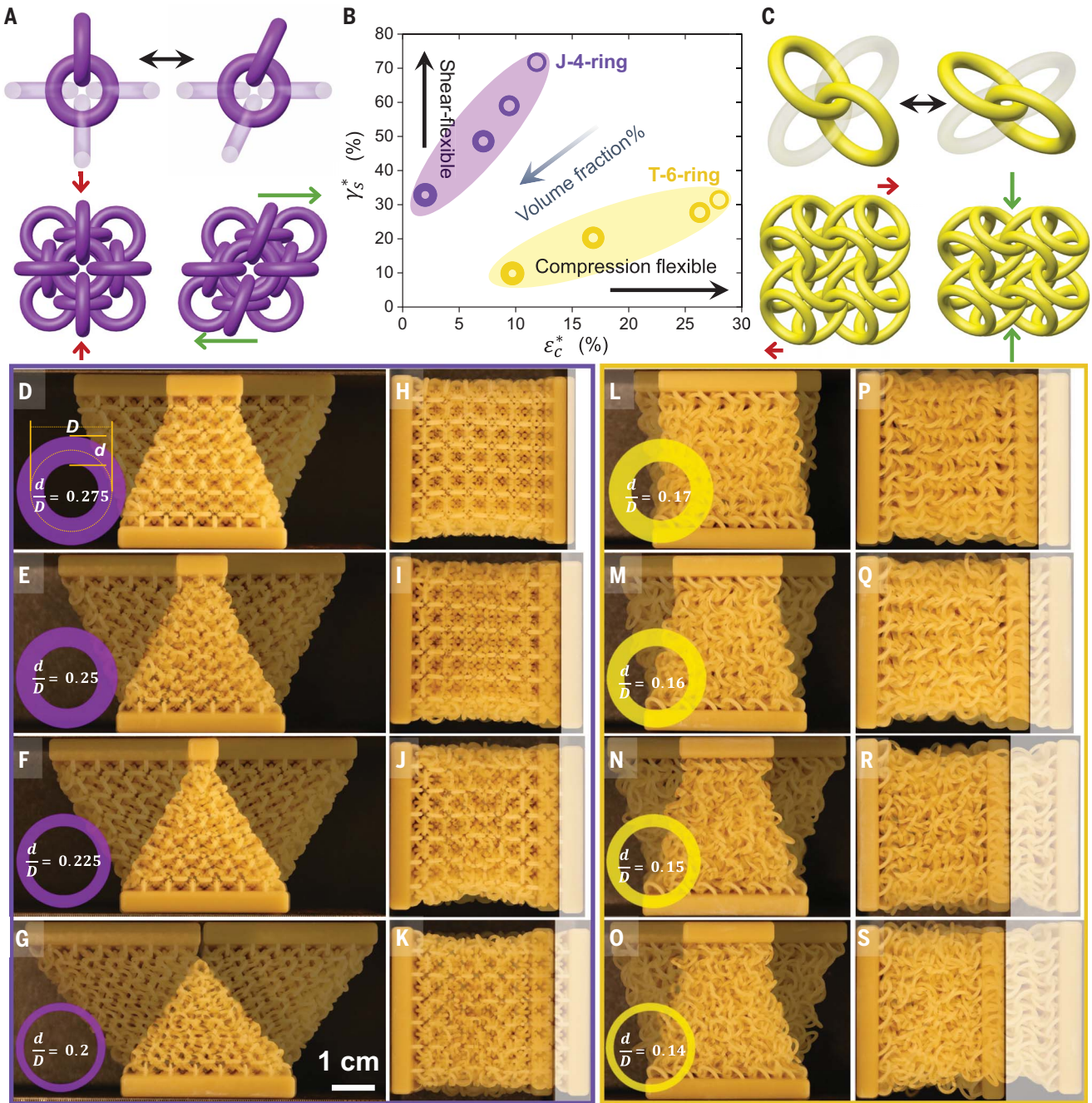


Fig. 4. Programmable critical jamming strains of PAMs. (A and C) The schematics illustrate the local ring arrangements under shearing and compressive loads for J-4-ring and T-6-ring PAMs, respectively. (B) A summary plot displaying critical shear jamming strain (γ_s^*) against the critical compressive jamming strain (ϵ_c^*) for both types of PAMs containing rings with varied thicknesses. (D to S) Photographs showing J-4-ring [(D) to (K)] and T-6-ring [(L) to (S)] PAMs at their corresponding critical jamming strains.

We constructed digital twins, replicating the ring's shape, density, size, and spatial arrangement, as well as the total number of rings in each respective sample.

All simulations qualitatively capture the inflection of η^* observed in experiments (compare Fig. 3, I and K with Fig. 3, E and H). Our simulations also agree with experiments in that the value of η^* at the inflection point is smaller for the J-4-ring sample compared with

that for the T-6-ring sample. However, our simulations overestimate the angular frequency at which the inflection of η^* happens. This mismatch could be due to imprecisions in the 3D-printed particle geometry and to contact imperfections, which are not included in our models. These discrepancies can also lead to considerable differences in particles' frictional interactions as well as the sample's packing structure in the relaxed configuration in experiments and sim-

ulations, which can shift the angular frequency at which the inflection of η^* happens. Nevertheless, our simulations provide particle-scale details that allow us to better understand the mechanisms underpinning this thinning-to-thickening transition. More specifically, from the point view of the rheophysics of dense granular materials (45–47), η^* takes contribution from two components: a contact component (which corresponds to percolating and

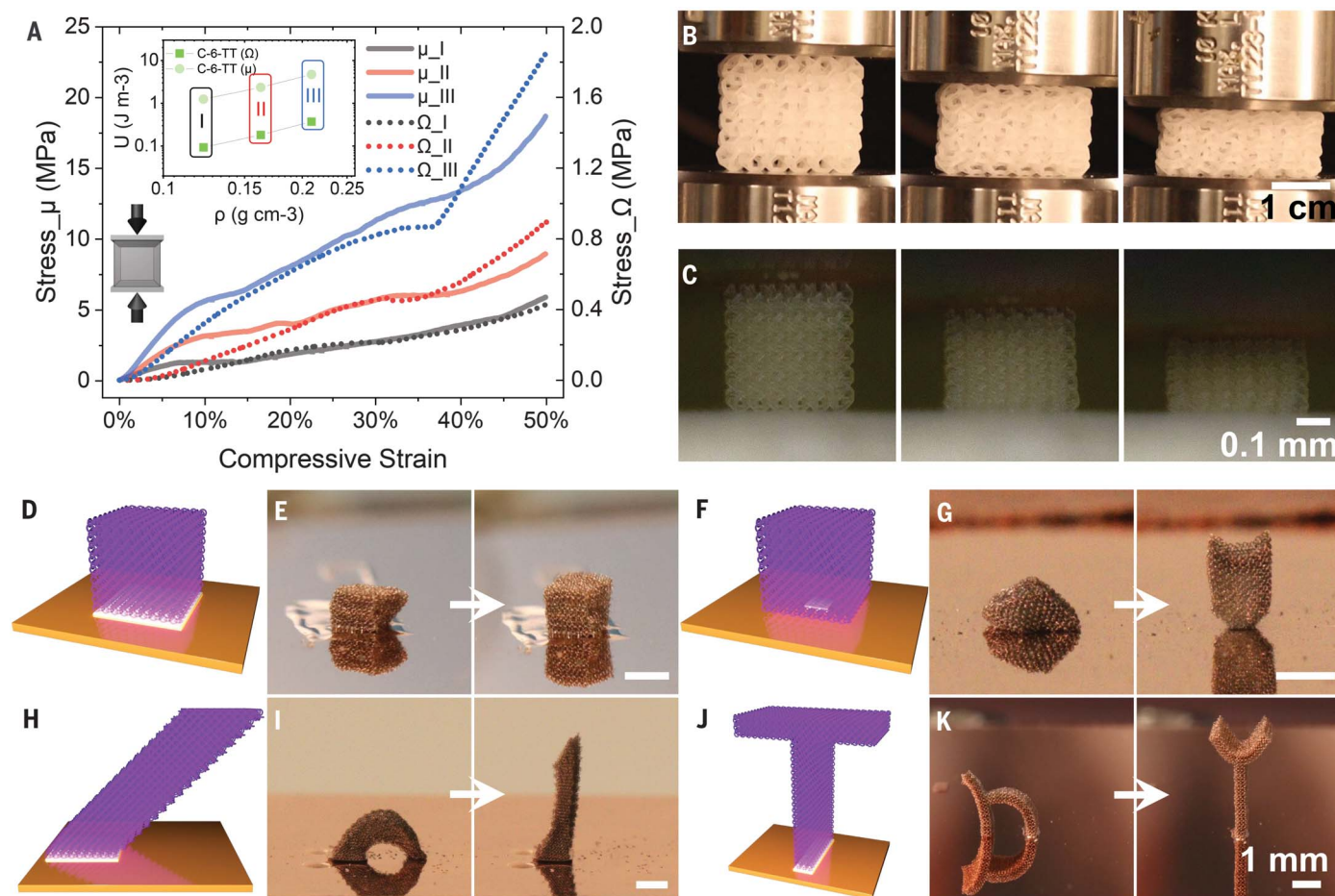


Fig. 5. Scale independence of PAMs and electrostatic actuation of μ -PAMs. (A) Stress-strain curves of C-6-TT PAMs fabricated at different scales (60 times difference in all dimensions) and volume fractions (III > II > I). Inset shows a comparative summary of energy absorption capacities of PAMs at two scales. (B and C) Snapshots of macroscale and microscale (B) C-6-TT PAMs undergoing compression experiments at strains of 0, 25, and 50%. Scale bars, 1 cm (B), 0.1 mm (C). (D to K) The J-4-ring μ -PAMs in various geometries, including cubes and letters, before and after electrostatic expansion. White regions in illustrations highlight the fixing area between the μ -PAMs and the substrate. These μ -PAMs, when subjected to electrostatic charges generated by a Van de Graaff generator, deploy from a relaxed natural state to an expanded state because of interparticle electrostatic repulsion. Scale bars, 1 mm.

enduring force chains in the statics of granular media, used often in the soil mechanics community) and a fluctuation component (which corresponds to the degree of turbulence of granular flow stemming from short-lived particle collisions, used often in the fluid mechanics community).

In our experiments, as the excitation frequency increases, we expect that both samples experience a transition from a contact-dominant (or “quasistatic”) regime to a fluctuation-dominant (or “inertia”) regime. As such, the initial decrease of η^* may be understood as the decrease of contact (due to stronger centrifugal effects) in the contact-dominant regime, whereas the later increase of η^* can be understood as the increased degree of “turbulence” (due to a faster external excitations) in the fluctuation-dominant regime. This concept is confirmed by looking at Fig. 3I (inset), which shows, for the simulation of the J-4-ring sample, the variation of the average contact num-

ber per particle and of the normalized average particle velocity fluctuation, δv [computed as the square root of granular temperature (45); see (37) for our calculation procedure], as functions of the angular frequency. As the angular frequency increases, the average contact number per particle decreases while the particle velocity fluctuation increases. In particular, the latter shows a much rapid increase rate once it exceeds the frequency of the inflection point of η^* , which suggests the transition from the contact-dominant regime to the fluctuation-dominant regime. A similar observation can be made for the T-6-ring sample by looking at Fig. 3K (inset) and comparing it with Fig. 3I (inset). According to kinetic theory (48), the viscosity of granular flow, η , depends on the density and granular temperature through a scaling $\eta \sim (\rho_c - \rho)^{-\alpha} \delta v$, where ρ_c is the material density at random close packing, ρ is the material density at a given flow state, and α is a scaling exponent whose value depends on

particle properties (such as shape and surface friction). We tested the relevance of this theory in describing the rheological response of PAMs. Due to difficulties in calculating objectively ρ for our simulated PAM samples, we used the mean contact number $\langle Z \rangle$ in place of ρ (with Z_c the contact number at random close packing), assuming that a power-law scaling between ρ and $\langle Z \rangle$ can translate from conventional granular materials (46) to PAMs. Figure 3J and Fig. 3L show the variation of the normalized viscosity, $\frac{\eta}{\delta v}$, as a function of $Z_c - \langle Z \rangle$ for the J-4-ring sample and the T-6-ring sample, respectively. We observed that in the low-excitation frequency regime (before the inflection of η^*), the rheological response follows a power-law scaling (black dashed line in Fig. 3, J and L) as predicted by kinetic theory. However, as it progresses into the high-frequency domain (after the inflection of η^*), the rheological response deviates further away from the respective power-law scaling

(insets of Fig. 3, J and L). The exact reason for this deviation is unknown, but one possible cause is the breakdown of the power-law scaling between $\langle Z \rangle$ and ρ in the high-frequency domain due to the presence of tensile contact (for preventing particles from separating) that is absent in conventional granular materials. Lastly, we note that Z_c is unknown for PAMs. For the results shown in Fig. 3, J and L, we used the mean contact number of the sample before the torsion experiment (that is, after gravity settlement) as an estimation of Z_c . A different Z_c will change the scaling exponent presented in Fig. 3, J and L, but it will not change the observed power-law relation.

Programmable critical jamming strains

We studied the role of particle geometry and particle linking topology in the jamming transition in PAMs. The local catenation topologies in PAMs play a pivotal role in defining their mesoscale (e.g., cell-to-cell, layer-by-layer) DOF, which, in turn, dictates the critical strain for jamming (ϵ_c^* : critical compressive jamming strain; γ_s^* : critical shear jamming strain). For instance, J-4-ring PAMs show a substantially higher γ_s^* as compared with T-6-ring PAMs, whereas T-6-ring PAMs exhibit a higher ϵ_c^* relative to J-4-ring PAMs. In J-4-ring PAMs, shear loading induces a coordinated rearrangement of particles, thereby amplifying γ_s^* (Fig. 4A). During this process, rings oriented parallel to the shearing direction maintain their orientations, while those perpendicular to the shearing direction rotate in a coordinated manner, facilitating a greater γ_s^* . However, under compression or tension, the rings' inability to adjust their positions—restricted by limited DOF from neighboring particles—results in a reduced ϵ_c^* . By contrast, T-6-ring PAMs rely on a “scissor” mechanism (Fig. 4C): Upon compressive loading, all rings adjust their orientations coordinatively, which allows for a larger ϵ_c^* .

In addition to the choice of catenation topology, the thickness, d , of the torus substantially influences the jamming transition in PAMs (Fig. 4D). A decrease in d generally correlates with an increased DOF in PAMs. To elucidate this relationship, we fabricated a series of J-4-ring and T-6-ring PAMs with constant ring diameters (D) but varied d . We measured the critical jamming strain under both shear (γ_s^*) and compressive (ϵ_c^*) loading conditions as a function of thickness d (Fig. 4B). Regardless of the catenation topology, reductions in d are associated with increases in both γ_s^* and ϵ_c^* . Furthermore, we observed that catenation topology significantly impacts the predominant deformation modes. For instance, the γ_s^* for J-4-ring PAMs (Fig. 4D), which exhibit the largest d/D ratio and therefore the lowest DOF, is higher compared with that of T-6-

ring PAMs (Fig. 4O), which have a much lower d/D ratio.

Length-scale dependence and electrostatic reconfiguration of μ -PAMs

The deformability of PAMs is primarily influenced by their particle geometries and the particle-to-particle DOF, which are expected to be scale-independent. Hence, we hypothesized that reducing the particle size by a factor of about 60 will retain the characteristic mechanical response of macroscopic systems, such as their quasistatic compressive behavior and liquid-fluid duality. To validate this hypothesis, we fabricated PAMs by using two-photon lithography with postprinting oxygen plasma etching (37). Upon completion of the fabrication and release process—during which plasma etching removes thin support materials required during fabrication—the μ -PAMs demonstrated a gravitational relaxation analogous to that observed in their macroscopic counterparts (fig. S17). We designed a series of C-6-TT PAMs (as in fig. S9), varying their volume fractions by changing the beam thicknesses of the particles. After an increasing order of beam thickness, we labeled the PAMs as I, II, and III (fig. S9). The same PAMs were fabricated at both macroscale (Ω_I , Ω_{II} , and Ω_{III}) and microscale (μ_I , μ_{II} , and μ_{III}), scaling them by a factor of 60 in all dimensions (i.e., sample side lengths: 24 mm and 400 μ m). Due to the differences in fabrication methods, we used slightly different acrylic polymers (37) for the macro- and microscale samples. Nevertheless, we found qualitative agreement between the mechanical responses of PAMs across scales (Fig. 5, A to C). The energy-absorption capacities of all C-6-TT PAMs were calculated by integrating the areas under the stress-strain curves. Our experiments revealed scale factors (U_μ/U_Ω) among all I, II, and III designs to be near constant at 12.76 ± 0.53 (Fig. 5A).

One defining difference between microscale and macroscale PAMs is their dramatically different surface-to-volume ratio (~60 times larger in the μ -PAM samples) and the reduced weight of each particle in the catenated network (a reduction by a factor of ~216,000 in the μ -PAM samples). Such discrepancy can be exploited to observe the role of interparticle forces (e.g., electrostatic repulsion) in the global deformation of PAMs. To test this hypothesis, we tessellated J-4-ring μ -PAM voxels to form various geometries: a side-anchored cube (Fig. 5D), a point-anchored cube (Fig. 5E), a bottom-anchored numeral “1” (Fig. 5F), and a bottom-anchored letter “T” (Fig. 5G). We then coated each μ -PAM sample with a thin layer of copper, approximately 300 nm in thickness, to provide electrical conductivity. We then positioned the samples atop a Van de Graaff generator with direct electrical contact (fig. S17). As electrostatic charges accumulated, the in-

dividual rings within the μ -PAMs began to repel each other because of increased electrostatic repulsion. This electrostatic interaction prompted the μ -PAMs to both expand outward in all directions owing to inter-ring repulsion and to elongate upwards owing to repulsion between the μ -PAMs and the substrate against gravity, transforming each initially collapsed structure into a structurally deployed state (Fig. 5, D and G, and movie S6). The charged μ -PAMs will stay in this deployed geometry until we discharge the Van de Graaff generator by neutralizing the electrical charge stored in its metallic dome, to which the conductive substrate of the μ -PAM samples is attached. The transition between the uncharged, compact state and the charged, deployed state was fast (<0.1 s; movie S9) and completely reversible. This behavior is derived from the fluid-solid duality also observed in the macroscale samples. Global deformations are allowed by the intrinsic DOF but constrained when reaching the tensile critical jamming strains, resulting in a “lockable” 3D shape-morphing behavior. This suggests that μ -PAMs driven by electrostatic forces can be engineered as responsive elements in remotely actuated materials for use in microscale devices and smart material systems.

Conclusions

We introduce PAMs as a class of architected materials that bridge the gap between discrete granular materials and continuous architected materials within a 3D domain. Our design strategy rationally maps discrete, topologically interlocked particles onto 3D crystalline networks. Their nonlinear elastic response in the jammed state, coupled with non-Newtonian shear-thinning and shear-thickening behaviors in the unjammed state, provides a versatile mechanical platform for applications requiring adaptive stiffness and energy dissipation. This is particularly relevant for stimuli-responsive materials, soft robotics, and morphing architectures. The material behavior of PAMs is highly dependent on their catenation topologies and particle geometries, which together determine the interparticle DOF. Depending on the target mechanical performance, different PAMs may fulfill different roles. For example, in applications that require large deformations, such as shape morphing and soft actuation, topologies with larger shear deformability (such as the J-4-ring) are preferable. Applications requiring larger energy absorption favor PAMs with higher compressive critical jamming responses (such as the T-6-ring), which also show relevant strain-stiffening characteristics. Lastly, for structural applications, stiffer PAMs are more advantageous. These are best represented by PAMs with J topologies using polygonal or polyhedral particle geometries (e.g., J-4-square and J-4-OCT). This work lays the foundation

for creating architected materials with unprecedented control over mechanical properties and responsiveness. Future research could address the resilience of these materials to discrete particle fracturing and examine their dynamic and wave propagation response, non-linear rheology, and thermal and optical characteristics, as well as look at optimal selection of constitutive materials and particle coatings, in order to target specific applications.

REFERENCES AND NOTES

1. A. J. D. Shaikkea, H. Cui, M. O'Masta, X. R. Zheng, V. S. Deshpande, *Nat. Mater.* **21**, 297–304 (2022).
2. X. Zheng *et al.*, *Science* **344**, 1373–1377 (2014).
3. R. Xue *et al.*, *Extreme Mech. Lett.* **40**, 100918 (2020).
4. K. Davami *et al.*, *Nat. Commun.* **6**, 10019 (2015).
5. O. Al-Ketan, A. Soliman, A. M. AlQubaisi, R. K. Abu Al-Rub, *Adv. Eng. Mater.* **20**, 1700549 (2018).
6. O. Al-Ketan, R. K. Abu Al-Rub, *Adv. Eng. Mater.* **21**, 1900524 (2019).
7. J.-F. Ganghoffer, A. Wazne, H. Reda, *Mech. Res. Commun.* **130**, 104114 (2023).
8. S. Arabnejad, D. Pasini, *Int. J. Mech. Sci.* **77**, 249–262 (2013).
9. K. Liu, R. Sun, C. Daraio, *Science* **377**, 975–981 (2022).
10. M. Zaiser, S. Zapperi, *Nat. Rev. Phys.* **5**, 679–688 (2023).
11. M. Kadic, G. W. Milton, M. van Hecke, M. Wegener, *Nat. Rev. Phys.* **1**, 198–210 (2019).
12. R. Lakes, *Science* **235**, 1038–1040 (1987).
13. S. Babaei *et al.*, *Adv. Mater.* **25**, 5044–5049 (2013).
14. T. Frenzel, M. Kadic, M. Wegener, *Science* **358**, 1072–1074 (2017).
15. J. Boddapati, M. Flaschel, S. Kumar, L. De Lorenzis, C. Daraio, *J. Mech. Phys. Solids* **181**, 105471 (2023).
16. B. Florijn, C. Coulais, M. van Hecke, *Phys. Rev. Lett.* **113**, 175503 (2014).
17. K. Bertoldi, V. Vitelli, J. Christensen, M. van Hecke, *Nat. Rev. Mater.* **2**, 17066 (2017).
18. C. Coulais, A. Sabbadini, F. Vink, M. van Hecke, *Nature* **561**, 512–515 (2018).
19. X. Xia *et al.*, *Nature* **573**, 205–213 (2019).
20. X. Xia, C. M. Spadaccini, J. R. Greer, *Nat. Rev. Mater.* **7**, 683–701 (2022).
21. S. Shan *et al.*, *Adv. Mater.* **27**, 4296–4301 (2015).
22. B. Haghpanah, L. Salari-Sharif, P. Pourrajab, J. Hopkins, L. Valdevit, *Adv. Mater.* **28**, 7915–7920 (2016).
23. S. Li, H. Fang, S. Sadeghi, P. Bhovad, K. W. Wang, *Adv. Mater.* **31**, e1805282 (2019).
24. J. Liu *et al.*, *Adv. Mater.* **28**, 6619–6624 (2016).
25. M. Kadic, T. Bückmann, N. Stenger, M. Thiel, M. Wegener, *Appl. Phys. Lett.* **100**, 191901 (2012).
26. T. Bückmann, M. Thiel, M. Kadic, R. Schittny, M. Wegener, *Nat. Commun.* **5**, 4130 (2014).
27. Y. Estrin, A. V. Dyskin, E. Pasternak, *Mater. Sci. Eng. C* **31**, 1189–1194 (2011).
28. C. Chong, M. A. Porter, P. G. Kevrekidis, C. Daraio, *J. Phys. Condens. Matter* **29**, 413003 (2017).
29. A. N. Karuriya, F. Barthelat, *Proc. Natl. Acad. Sci. U.S.A.* **120**, e2215508120 (2023).
30. Y. Wang, L. Li, D. Hofmann, J. E. Andrade, C. Daraio, *Nature* **596**, 238–243 (2021).
31. P. Tang, S. Coros, B. Thomaszewski, *ACM Trans. Graph.* **42**, 1–12 (2023).
32. Y. Liu, M. O'Keeffe, M. M. J. Treacy, O. M. Yaghi, *Chem. Soc. Rev.* **47**, 4642–4664 (2018).
33. L. Carlucci, G. Ciani, D. M. Proserpio, *Coord. Chem. Rev.* **246**, 247–289 (2003).
34. M. O'Keeffe, M. M. J. Treacy, *Int. J. Topol.* **1**, 1–10 (2024).
35. T. S. Lumpe, T. Stankovic, *Proc. Natl. Acad. Sci. U.S.A.* **118**, e2003504118 (2021).
36. Reticular Structure Chemistry Resource (RCSR) (2024); <http://rcsr.net/>.
37. Materials and methods are available as supplementary materials.
38. E. Brown, A. Nasto, A. G. Athanassiadis, H. M. Jaeger, *Phys. Rev. Lett.* **108**, 108302 (2012).
39. R. Kawamoto, E. Andò, G. Viggiani, J. E. Andrade, *J. Mech. Phys. Solids* **91**, 1–13 (2016).
40. R. Kawamoto, E. Andò, G. Viggiani, J. E. Andrade, *J. Mech. Phys. Solids* **111**, 375–392 (2018).
41. L. Li, E. Marteau, J. E. Andrade, *Granul. Matter* **21**, 43 (2019).
42. A. J. Liu, S. R. Nagel, *Annu. Rev. Condens. Matter Phys.* **1**, 347–369 (2010).
43. T. C. de Goede, K. G. de Bruin, D. Bonn, *Sci. Rep.* **9**, 1250 (2019).
44. H. M. Laun, *Angew. Makromol. Chem.* **123**, 335–359 (1984).
45. C. K. K. Lun, S. B. Savage, D. J. Jeffrey, N. Chepur, *J. Fluid Mech.* **140**, 223–256 (1984).
46. F. da Cruz, S. Emam, M. Prochnow, J.-N. Roux, F. Chevoir, *Phys. Rev. E Stat. Nonlin. Soft Matter Phys.* **72**, 021309 (2005).
47. L. Li, J. E. Andrade, *Granul. Matter* **22**, 52 (2020).
48. W. Losert, L. Bocquet, T. C. Lubensky, J. P. Gollub, *Phys. Rev. Lett.* **85**, 1428–1431 (2000).

ACKNOWLEDGMENTS

We thank M. L. Hunt, R. X. Fu, T. Zhou, and J. Boddapati for discussions.

Funding: W.Z. and C.D. acknowledge support from the Gary Clinard Innovation Fund and the Army Research Office (MURI ARO W911NF-22-2-0109). Computational resources were provided by the High-Performance Computing Center at Caltech. A.G.I. and X.X. acknowledge the financial support from Lawrence Livermore National Laboratory's (LLNL) Lab Directed Research and Development Program (22-ERD-004). Work at LLNL was performed under the auspices of the US Department of Energy by LLNL under contract DE-AC52-07NA27344. **Author contributions:** W.Z. and S.N. contributed equally. W.Z. and C.D. conceived the idea. W.Z. designed the structures and fabricated the samples. W.Z., S.N., and C.D. designed the experiments. S.N., W.Z., A.K.P., and P.P. performed the experiments and analyzed experimental data. L.L. and H.Y. performed numerical simulations and analyzed simulation data. X.X. and W.Z. designed the microscale experiments. X.X. and A.G.I. fabricated and tested microscale samples. W.Z. and C.D. wrote the initial draft. All authors interpreted the results and reviewed the manuscript. **Competing interests:** The authors declare that they have no competing interests. **Data and materials availability:** All data are available in the main text or the supplementary materials. Other information related to this study is available from the corresponding author upon reasonable request. **License information:** Copyright © 2025 the authors, some rights reserved; exclusive licensee American Association for the Advancement of Science. No claim to original US government works. <https://www.science.org/about/science-licenses-journal-article-reuse>

SUPPLEMENTARY MATERIALS

science.org/doi/10.1126/science.adr9713

Materials and Methods

Supplementary Text

Figs. S1 to S25

Tables S1 and S2

References (49–60)

Movies S1 to S9

Submitted 24 July 2025; accepted 11 November 2024

10.1126/science.adr9713